Nano Research

Open Access

Research Article

Inorganic all-solid-state composite structure for dynamic color

Xinting Li[1,2], Jiancun Zhao[1,2] ✉, Junyi Yang[1,2], Yuhao Guo[1,2], Yihui Huo[1,2], Wenli Li[1,2,3], and Yiting Yu[1,2] ✉

[1] *Ministry of Education Key Laboratory of Micro/Nano Systems for Aerospace, Key Laboratory of Micro/Nano Systems for Aerospace, Key Laboratory of Micro- and Nano-Electro-Mechanical Systems of Shaanxi Province, School of Mechanical Engineering, Northwestern Polytechnical University, Xi'an 710072, China*

[2] *Key Laboratory of Scale Manufacturing Technologies for High-Performance MEMS Chips of Zhejiang Province, Key Laboratory of Optical Microsystems and Application Technologies of Ningbo City, Ningbo Institute of Northwestern Polytechnical University, Ningbo 315103, China*

[3] *Key Laboratory of Advanced Process Control for Light Industry (Ministry of Education), Jiangnan University, Wuxi 214122, China*

Cite this article: *Nano Research*, **2026**, *19*, 94908612. https://doi.org/10.26599/NR.2026.94908612

ABSTRACT: Dynamic color modulation holds great promise for next-generation display technologies, offering wide applicability in smart displays, adaptive surfaces, and wearable electronics. However, conventional WO_3-based electrochromic (EC) devices face inherent limitations, making it difficult to simultaneously achieve broad color tunability and rapid response performance. Here, we proposed an inorganic all-solid-state composite structure that synergistically integrates structural color and WO_3-based EC modulation via color superposition. The underlying $Ag/Al_2O_3/Ni/Al_2O_3$ stack provides static structural coloration, while the top $ITO/WO_3/LiTaO_3/NiO/ITO$ stack enables dynamic, voltage-controlled color tuning. The resulting composite structure achieves precise, reversible color modulation under 1.5 V, with colored and bleached times of 2.5 and 1 s, respectively, and excellent stability over 1000 cycles. After applying the voltage to induce coloration, the device can maintain its colored state without a continuous power supply, demonstrating the intrinsic non-volatile EC behavior. This integrated approach effectively overcomes the narrow color range and sluggish switching of conventional WO_3-based EC systems, providing a simple-to-fabricate, versatile, and energy-efficient platform for high-performance adaptive optical devices. Looking ahead, extending the color tunability of EC layers or introducing multiple EC modulation layers could further expand the dynamic color range, paving the way for multicolor, reconfigurable reflective displays and smart optical systems.

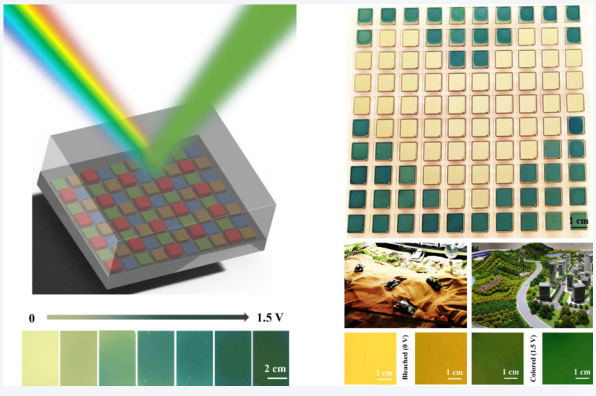

KEYWORDS: dynamic color, composite structure, structural color, electrochromic, WO_3

1 Introduction

Dynamic modulation of color is an increasingly prominent topic in contemporary research, drawing significant interest across various scientific disciplines. Beyond its applications in optical devices, dynamic color technology is poised to impact a wide range of fields, including display technology, anti-counterfeiting measures, sensors, smart textiles and wearables, decorative materials, architectural design, biomedicine, and energy solutions [1–8]. Currently, colors arising from interference effects, plasmonic resonances, and Mie resonances can be dynamically modulated via distinct physical and electrochemical mechanisms [9, 10]. Representative strategies include electrochromic (EC) modulation, which is typically associated with reversible electrochemical redox and charge-transfer processes, refractive-index or lattice-parameter modulation in photonic crystal structure, and electric-field-induced molecular reorientation in liquid-crystal systems [11–17]. Each strategy exhibits distinct advantages and limitations, with their applicability largely determined by the nature of the external stimuli, such as electric fields, thermal variations, or mechanical deformations [18–24]. Among them, inorganic EC technologies stand out for their superior reversible color modulation performance, owing to their long operational lifetime, excellent bistability (power-off memory effect), and low energy consumption, making them a promising technology for diverse applications [25–28]. However,

Received: November 15, 2025; **Revised:** January 14, 2026
Accepted: March 2, 2026

✉Address correspondence to Jiancun Zhao, zhaojiancun@nwpu.edu.cn; Yiting Yu, yyt@nwpu.edu.cn

limitations of inorganic EC devices include less color, slow response speed (over several seconds or even tens of seconds), etc. [29]. Therefore, optimizing the performance of inorganic EC devices requires the rational design of geometric structures, as well as the careful selection and preparation of materials.

WO_3, as a common cathode EC oxide material, has been widely studied for the design of inorganic EC devices [30–33]. High coloring efficiency, excellent cyclic stability, and stable ion embedding are some of its benefits. Its color change originates from a redox process involving ion intercalation into the material's lattice, typically leading to a transparent-to-blue transition [34, 35]. For example, a recently reported fully inorganic, all-solid-state WO_3-based EC device based on oxygen-vacancy tungsten oxide functionalized with zinc oxide (O_V-WO_{3-x}/ZnO) composite films exhibits a reversible EC color transition from colorless to blue under an applied voltage, together with a large optical modulation and second-scale coloration/bleaching dynamics [36]. This work demonstrates the practical feasibility and structural robustness of fully inorganic, all-solid-state WO_3-based EC devices. In response to the growing demand for dynamic multicolor applications, increasing research efforts have been devoted to developing advanced multicolor design strategies for WO_3-based EC devices through geometric structure engineering [37, 38]. For instance, the combination of W and WO_3 thin films with Fabry–Pérot (FP) cavities enables dynamic modulation of multicolor, resulting in high contrast and color purity [39–41]. Additionally, an electrically switchable full-color palette based on WO_3 nanostructures has been demonstrated, offering a wide color gamut with dynamic on–off switching under applied voltage [42]. However, despite their demonstrated multicolor capability, these approaches still face practical limitations, including relatively slow response speeds (often > 10 s), increased driving voltages, dependence on liquid or polymer electrolytes, and difficulties in achieving robust device integration and long-term stability. In summary, achieving both high-quality color modulation and fast response remains difficult in reported WO_3-based EC devices.

Herein, we proposed and demonstrated an inorganic all-solid-state composite structure for dynamic color that integrates structural color and WO_3-based EC technologies. The structural color layers are directly deposited onto a glass substrate as the base color layers, and the EC layers are directly deposited on top of the structural color layers. To minimize the impact on EC ion transmission efficiency, the structural color layers utilize a planar thin film structure. Accordingly, the $Ag/Al_2O_3/Ni/Al_2O_3$ stack functions as the structural color layers, producing vivid and stable colors via FP resonance. The EC layers composed of indium tin oxide (ITO)/WO_3/$LiTaO_3$/NiO/ITO serve to modulate the optical spectrum dynamically, exhibiting a reversible transition under electrical stimulation. Based on the principle of color superposition, the colors generated by the bottom structural color layers and the top EC layers are spectrally superimposed to produce a distinct and reversible color transition under electrical control. Specifically, the proposed composite structure exhibits a voltage-driven color change from yellow to green at 1.5 V, while maintaining rapid colored (2.5 s) and bleached (1 s) response times, as well as excellent stability over 1000 cycles. Moreover, the color change from yellow to green, mimicking the transition from desert to forest on land battlefields, illustrates the possibility of applying EC devices in the field of stealth and camouflage. In addition, this design scheme serves as a model for the creation of future high-quality dynamic multicolor devices by fusing structural color and EC elements into a composite structure based on color superposition.

2 Results and discussion

A conceptual diagram of our proposed inorganic all-solid-state composite structure, along with the color superposition design principle, is shown in Fig. 1. To achieve dynamic color modulation

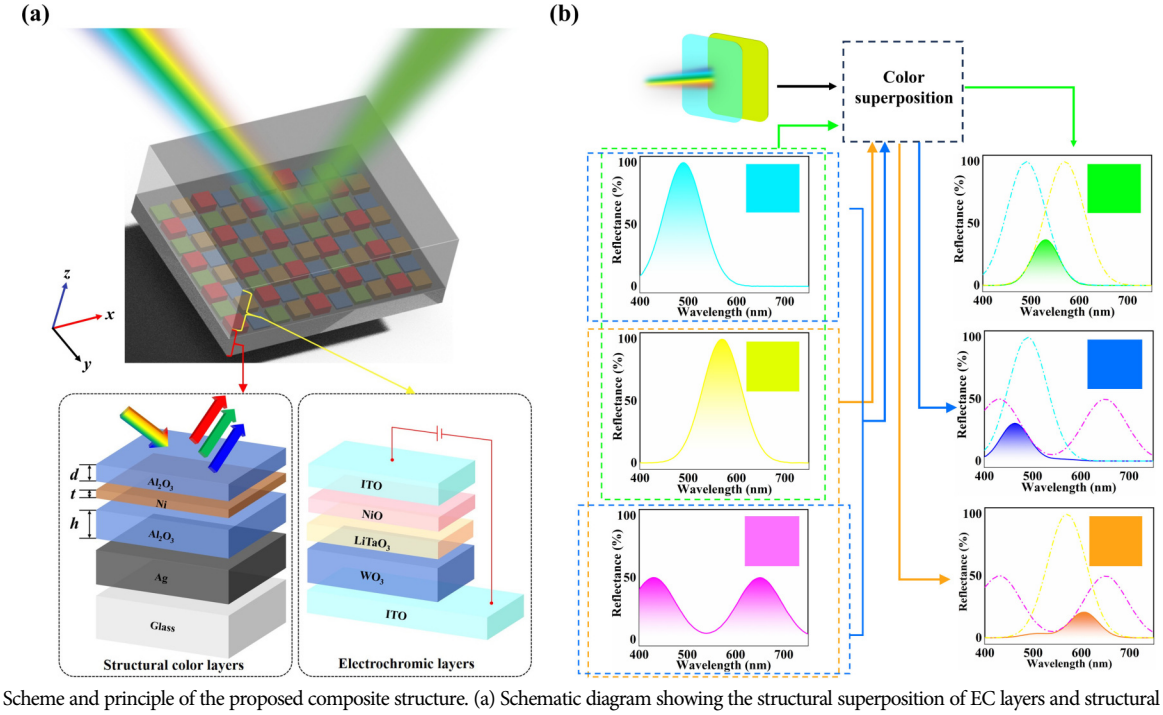

Figure 1 Scheme and principle of the proposed composite structure. (a) Schematic diagram showing the structural superposition of EC layers and structural color layers. (b) Based on color superposition, the approximate spectrum of three different colors, cyan, yellow, and magenta, is calculated after the spectra are superimposed. The illustration is the corresponding color block diagram.

with fast response, the thin-film structural color layers are employed as the bottom layers of the composite device, enabling highly saturated full-color output and ensuring compatibility with all-solid-state WO_3-based EC layers, thereby not hindering ion migration during the chemical process and maintaining the intrinsic EC performance. The top EC layers have dynamic adjustment capabilities and can switch from the bleached to the colored state after power is applied. For this composite structure with layers stacked and integrated, since the EC layers are almost transparent in the initial state, the original color output of the device is mainly determined by the bottom structural color layers. Dynamic color modulation via color superposition is realized as the EC layers introduce spectral modulation that couples with the reflective spectrum of the structural color layers, yielding a new composite color output. This strategy further optimizes the color control capability based on the single switching mode of "transparent-colored" (such as transparent to blue) of traditional WO_3-based EC devices.

To verify the feasibility of our proposed composite structure to realize dynamic color, we calculated the spectral superposition of several sets of two color layers based on the superposition strategy [43–45]. For instance, we used MATLAB to do superposition calculations after selecting the cyan, yellow, and magenta spectra, as shown in Fig. 1(b). The results indicate that combining cyan with yellow yields a green color, cyan with magenta produces a blue color, and yellow with magenta results in an orange hue, approximately. Analogously, by engineering multiple color layers, a wide range of target colors can be synthesized. Moreover, dynamic modulation of a single color layer can generate dynamic effects on the final output color. This also confirms the rationality of our designed composite structure for realizing dynamic multicolor devices, providing theoretical support for the experiment.

Structural color layers, serving as the core component of the proposed composite structure, play a pivotal role in generating vibrant and high-quality colors, forming the basis for dynamic color modulation. In contrast to many state-of-the-art structural color approaches that depend on complex three-dimensional nanostructures, lithographically defined metasurfaces, or highly ordered photonic crystals, the structural color layers employed in this work are realized using a simple planar multilayer thin-film configuration. This strategy enables vivid and spectrally well-defined colors through thin-film interference while substantially reducing structural complexity and fabrication requirements. Specifically, Ag serves as the reflective layer to ensure strong reflectance, Al_2O_3 functions as a dielectric spacer with low absorption and a moderate refractive index (Fig. S1 in the Electronic Supplementary Material (ESM)), providing both interference regulation and protection, while Ni introduces visible-light absorption to enhance color selectivity and purification. Importantly, all constituent materials (Ag, Al_2O_3, and Ni) are widely available, chemically stable, and compatible with standard thin-film deposition processes such as electron-beam (e-beam) evaporation or magnetron sputtering. This material system enables structural color generation through a simple planar multilayer structure without the need for nanolithography or complex patterning, thereby offering high scalability, large-area compatibility, and economic viability for practical implementation. As shown in Fig. 2(a), the light propagation process through the structural color layers is carefully engineered to create specific phase relationships, Eq. (1) as follows [46, 47]

$$\delta = \varphi_{prop} - (\varphi_a + \varphi_b) \quad (1)$$

where δ is the total phase accumulated during a single round-trip

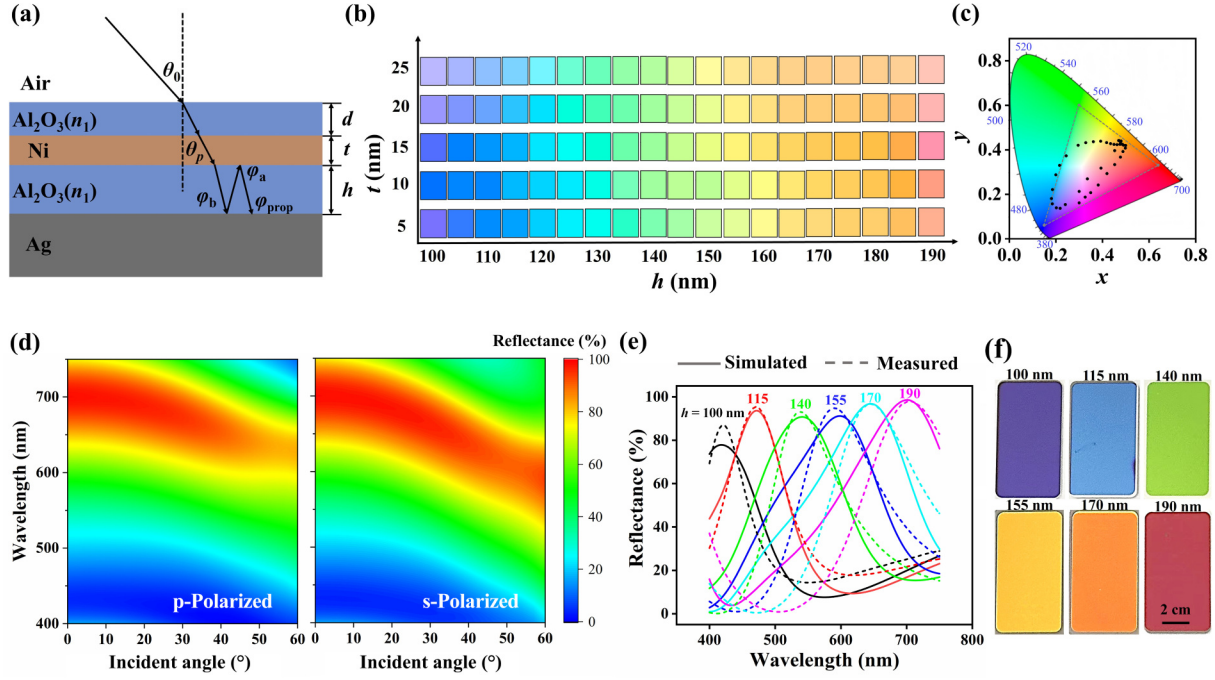

Figure 2 Performance demonstration of the structural color layers. (a) Schematics of theoretical analysis. (b) The simulated thickness variations of t and h match the relevant colors. (c) The simulated CIE chromaticity diagram with h changing. The gray line denotes sRGB color space. (d) Angular responses of the device obtained from simulation correspond to an angle of 0° to 60°, with the thickness h = 190 nm (the angular performance of other thicknesses h is shown in Fig. S5 in the ESM). (e) Simulated and measured reflectance spectra, where d, t, and the Ag reflective layer were fixed at 25, 15, and 200 nm, respectively, and h = 100, 115, 140, 155, 170, and 190 nm, respectively. (f) The actual sample image prepared has a thickness consistent with (e).

within the cavity, φ_a and φ_b represent the reflection phase shifts at the Ni/Al_2O_3 and Ag/Al_2O_3 interfaces, respectively. The phase shift due to round-trip propagation inside the cavity, φ_{prop} is given by Eq. (2)

$$\varphi_{prop} = \frac{4\pi n_1 h \cos(\theta_p)}{\lambda} \quad (2)$$

where n_1 is the refractive index of the medium inside the cavity, h is the thickness of the cavity, θ_p is the propagation angle of the light inside the cavity, and λ is the wavelength. Resonance occurs when $\delta = 2m\pi$, where m is an integer denoting the resonance order. The FP resonance effect within this multi-layered configuration allows for the fine-tuning of reflected wavelengths, resulting in vivid, high-contrast colors. By adjusting the thickness and refractive index of the layers, we can manipulate the optical response and optimize the device for high color saturation and stability across different angles of observation.

Building on the FP resonance mechanism described above, the optical response of the structural color layers is therefore highly sensitive to the geometric parameters of the thin-film stack, particularly the layer thicknesses. To systematically evaluate the influence of thickness variation on color performance, finite-difference time-domain (FDTD) simulations were carried out to analyze the optical behavior of the structural color layers. The top Al_2O_3 layer functions as an anti-reflection (AR) coating that suppresses undesired reflectance in off-resonant wavelength regions, thereby enhancing color purity and saturation. At the same time, it serves as a protective barrier for the underlying metal film, improving the environmental stability of the device. Based on systematic simulations in which the Al_2O_3 thickness d was varied from 0 to 50 nm, an optimal thickness of 25 nm was identified as a trade-off between minimizing off-resonant reflection and maintaining sufficient resonant reflectance, resulting in improved overall color performance (Figs. S2 and S3 in the ESM). The Ag layer serves primarily as an optically opaque reflector. Provided it is sufficiently thick to prevent transmission, variations in Ag thickness have minimal impact on the reflectance spectrum and resulting structural color. This was confirmed by simulations of Ag thickness ranging from 50 to 200 nm, which showed negligible changes in optical response (Fig. S4 in the ESM). Therefore, we selected 200 nm as the final thickness for the Ag reflective layer. To further explore the influence of structural parameters on the color output, we performed simulations varying the cavity thickness h and the Ni metal layer thickness t. The resulting color map, shown in Fig. 2(b), was derived from the simulated reflectance spectra. In these simulations, the thickness of layer t was varied from 5 to 25 nm in 5 nm increments, while layer h was varied from 100 to 190 nm with a step size of 5 nm. The simulation results indicate that varying the thickness of h enables precise tuning of the output hue, whereas adjusting the thickness of t primarily modulates the color saturation. Based on this analysis, a thickness of t = 15 nm was adopted in the structure design to achieve high color saturation. As shown in Fig. 2(c), the CIE 1931 chromaticity diagram corresponding to different h values demonstrates that the proposed structural color layers enable broad color-space coverage, spanning the primary and representative hues of the sRGB color space and providing vivid and continuously tunable colors. Additionally, the structural color layers exhibit angle insensitivity, maintaining consistent color across viewing angles up to 60° (Fig. 2(d) and Fig. S5 in the ESM), thereby underscoring the robustness of the proposed structure for practical applications requiring stable color performance from multiple perspectives. To further verify the feasibility, the reflectance spectra from experimental measurements were compared with simulations (Fig. 2(e)), where h = 100, 115, 140, 155, 170, and 190 nm, respectively. The strong agreement between measured and simulated spectra confirms the accuracy of the optical model, and the samples (Fig. 2(f)) fabricated by e-beam evaporation exhibit colors consistent with simulations, further verifying the practical viability of the design. Structural verification of the representative sample (h = 190 nm) is provided by the cross-sectional scanning electron microscope (SEM) image shown in Fig. S6 in the ESM.

For the EC layers responsible for regulating dynamic color changes, the structure is composed of five distinct layers: ITO/WO_3/$LiTaO_3$/NiO/ITO. The thickness of each EC layer was carefully optimized through a combination of experimental evaluation and theoretical considerations to balance optical modulation, response time, and cycling stability. Figure 3(a) presents the cross-sectional SEM image of the EC layers, fabricated by e-beam evaporation. Well-defined interfaces and uniform layer thicknesses are clearly observed, confirming precise thickness control and high structural integrity. The clear separation of each layer indicates the structural integrity required for optimal EC performance, ensuring that the device can achieve consistent and repeatable color changes over extended cycling. Notably, each layer plays a distinct functional role in the EC system. ITO acts as a transparent conductive electrode with high conductivity and optical transparency. NiO serves as the ion storage layer, with its thickness optimized to balance ion capacity and optical transparency in the bleached state. $LiTaO_3$ serves as the all-solid-state electrolyte layer, providing a stable reservoir of mobile Li^+ with high ionic conductivity, excellent electrochemical stability, and good compatibility with adjacent functional layers. Its solid-state nature effectively avoids issues associated with liquid electrolytes, such as leakage and integration complexity, thereby improving device reliability and cycling durability. WO_3 functions as the EC oxide layer and is one of the most widely used inorganic EC materials owing to its high chemical stability, well-defined redox activity, and large optical modulation capability. Under an applied voltage, WO_3 undergoes reversible electrochemical reactions, enabling stable and repeatable switching between colored and bleached states. The reaction process can be described by the following simplified chemical reaction (Eq. (3)) [48–50]

$$WO_3(\text{bleached}) + xLi^+ + xe^- \leftrightarrow Li_xWO_3(\text{colored}) \quad (3)$$

where x is the number of ions inserted into the WO_3 lattice ($0 \le x \le 1$) and e^- represents an electron. In this reaction, WO_3 undergoes electrochemically driven Li^+ intercalation under an applied voltage, forming Li_xWO_3 and leading to a reversible change in its optical properties. The intercalation of Li^+ induces enhanced visible-light absorption, resulting in the colored state of the film. Conversely, under a reversed bias, Li^+ deintercalation restores the original optical properties of WO_3 and yields the bleached, high-transmittance state. Based on this EC mechanism, it can be seen that the surface morphology of each functional layer is also intuitively important to the EC performance. Therefore, the surface morphologies of the individual functional layers and the complete EC layers were further characterized by SEM and atomic force microscope (AFM) (Figs. S7 and S8 in the ESM). The WO_3 film exhibits a dense and uniform surface with low roughness, which is

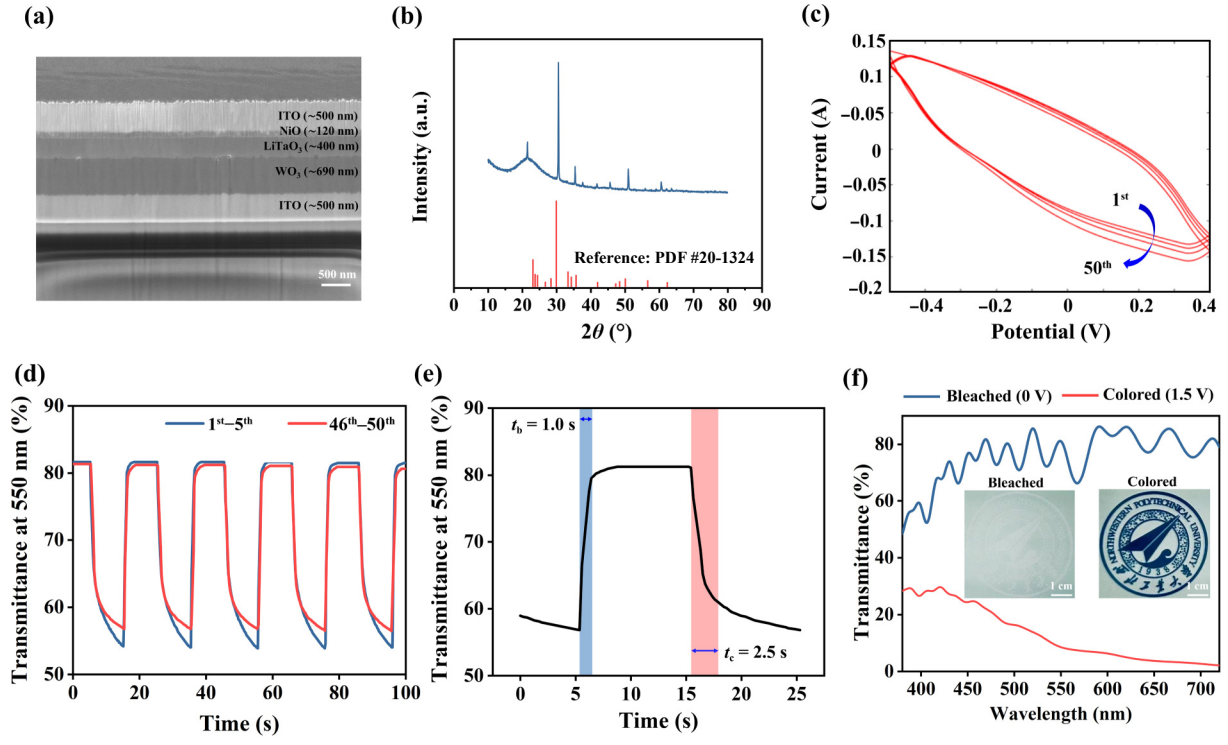

Figure 3 Performance demonstration of the EC layers. (a) SEM image of the side view of the EC layers. (b) XRD pattern of WO_3. (c) The CV curves of EC layers at 50 cycles. (d) Transmittance change timing diagram corresponding to wavelength 550 nm. (e) The response times of the EC layers at the transmittance of 550 nm. (f) Transmittance spectra of the EC layers in the bleached and colored states, along with corresponding optical images of the Northwestern Polytechnical University logo.

favorable for reversible Li^+ intercalation/deintercalation and long-term cycling stability. Similarly, the NiO ion-storage layer and the $LiTaO_3$ solid electrolyte layer show homogeneous, compact, and pinhole-free surfaces, ensuring stable electrochemical activity and efficient ion conduction. The complete EC layers also present good surface uniformity, confirming the high quality of the deposited films.

To ensure optimal EC functionality, the material quality and structural characteristics of the WO_3 thin film are of paramount importance. As part of the analysis, Fig. 3(b) presents the X-ray diffraction (XRD) pattern of a WO_3 thin film annealed at 300 °C on glass/ITO. The results exhibit well-defined diffraction peaks, suggesting good crystallinity of the WO_3 films, which is generally favorable for stable EC operation and long-term cycling performance. To further verify their durability, the EC layers were evaluated by cyclic voltammetry (CV), as shown in Fig. 3(c), exhibiting stable performance over 50 cycles without significant degradation. Meanwhile, the transmittance variation over 50 cycles, measured at a wavelength of 550 nm (Fig. 3(d)), which serves as a representative wavelength within the effective visible modulation range, further confirms the excellent stability of the EC layers. Additionally, Fig. 3(e) captures dynamic color response times, showing that the colored time remains at 2.5 s while the bleached time is 1 s. Collectively, the above results demonstrate that the EC layers sustain stable color transitions and fast switching behavior over prolonged cycling, indicating excellent electrochemical durability without noticeable performance degradation. This robustness confirms the reliability of the EC layers for dynamic and reversible optical modulation, highlighting their suitability for long-term applications requiring tunable optical properties.

Further, a patterned sample featuring the Northwestern Polytechnical University logo was fabricated via photolithography combined with e-beam evaporation, and its transmission spectrum was subsequently measured, as shown in Fig. 3(f). In the bleached state (no applied voltage), the logo remains visually concealed, blending seamlessly with the background. Upon applying a voltage of 1.5 V, the logo transitions into a distinct deep-blue state with enhanced visual contrast, which remains stable even after the voltage is removed. A video demonstrating this dynamic switching behavior is provided in Movie S1 in the ESM. This controllable visibility underscores the device's promise for information encryption and anti-counterfeiting applications, where selective optical appearance is critical. Furthermore, the measured transmittance spectra of the bleached and colored states reveal a reduction from 80% to 10% in average transmittance, indicating excellent optical modulation capabilities. Minor spectral fluctuations in the bleached-state transmittance are observed, which are commonly associated with multilayer thin-film structures.

Finally, the entire device, comprising a composite structure with the bottom structural color layers and the top EC layers, was fabricated via e-beam evaporation. Figure 4(a) compares the color change behavior of two sets of experimental samples—EC layers and the entire device—under applied voltages ranging from 0 to 1.5 V. The results show that the color change trend of the two sets of experimental samples is consistent with theoretical predictions: The blue hue induced by the EC layers combines with the underlying yellow structural color to produce a green appearance. As the applied voltage increases, the EC layers gradually transition from transparent to deeper blue tones, dynamically tuning the resulting color through controlled optical superposition with the structural color layers. The observed color transition is from yellow to green, and Movie S2 in the ESM contains a movie that illustrates this dynamic switching behavior. Furthermore, as shown in Fig. 4(b), the entire device consists of 1 cm × 1 cm samples

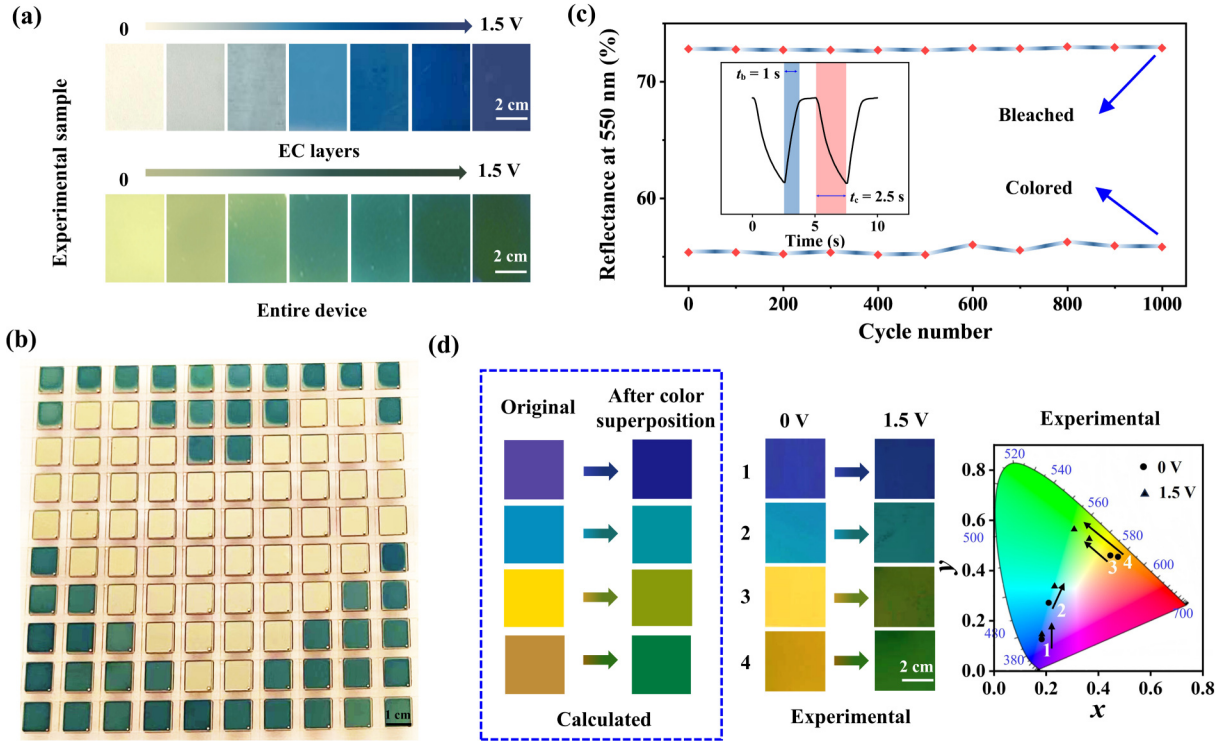

Figure 4 Performance demonstration of the entire device. (a) Dynamic color modulation images of the EC layers and the entire device when the voltage is changed from 0 to 1.5 V for two sets of experimental samples. (b) The entire device consists of 1 cm × 1 cm samples arranged in a 10 × 10 array, where selective voltage application to the small Ag contact electrodes enables patterned dynamic color transitions. (c) Response time and reflectance evolution at 550 nm with 1000 cycles of the entire device. (d) Color modulation of four experimental samples with distinct underlying structural colors under applied voltages of 0 and 1.5 V, along with their corresponding CIE 1931 chromaticity coordinates. For comparison, the calculated color (based on the design principle of Fig. 1(b)) variation of the same underlying color superimposed with a blue EC layer is provided as a reference.

arranged in a 10 × 10 array, which was realized using deposition masks to demonstrate the overall dynamic color modulation effect, where each sample was equipped with the small Ag contact electrodes deposited on the top ITO layer for electrical addressing. By selectively applying voltages to individual samples, dynamic color transitions can be locally induced, enabling the target pattern. Additionally, to demonstrate that the integration of the structural color and EC layers maintains functional stability under color superposition, the entire device was evaluated for EC performance. As shown in Fig. 4(c), the reflectance variation at 550 nm and the response times (2.5 s for colored and 1 s for bleached) remain stable even after 1000 cycles, confirming that the integration does not compromise response speed or cycling stability. A quantitative comparison with previously reported EC devices, summarized in Table S1 in the ESM, further highlights the competitive overall performance of the proposed device.

To verify that the composite structure can also achieve dynamic modulation of more colors, Fig. 4(d) illustrates the voltage-dependent color modulation (0 and 1.5 V) of four experimental samples from the entire device. Corresponding cross-sectional SEM images of these samples are provided in Fig. S9 in the ESM, clearly illustrating the multilayer structure and interfaces. The calculated color variation of the same underlying color in superposition with a blue EC layer is included as a reference. A satisfactory consistency is observed between the experimental and calculated results. The CIE 1931 chromaticity coordinate diagram further illustrates that the extent of coordinate shifts under applied voltage reflects the dynamic modulation amplitude of the four experimental samples, confirming that the proposed design enables color transitions across regions such as blue, yellow, and green. This demonstrates that integrating structural color layers with EC layers markedly broadens the achievable dynamic color range. In addition, the reversible color transition from yellow to green closely resembles natural variations in environmental coloration, such as the visual shift from desert terrain to forest or grassland vegetation. As shown in Fig. S10 in the ESM, this color transition exhibits good visual consistency with corresponding changes in the simulated environment. These results suggest that the proposed composite structure has promising potential for adaptive camouflage and stealth-related applications.

3 Conclusions

In summary, we have proposed and experimentally demonstrated an inorganic all-solid-state composite structure that enables dynamically tunable reflective coloration through the integration of multilayer structural color and WO_3-based EC modulation. The device is fabricated using a simple and scalable thin-film deposition process. The fabricated device exhibits a reversible color transition from yellow to green under a voltage of 1.5 V, with colored and bleached times of 2.5 and 1 s, respectively, and demonstrates excellent cycling stability even after 1000 cycles, as verified by reflectance spectra. The results confirm that the combination of structural color layers and EC layers not only preserves response speed and stability but also significantly increases the achievable color modulation.

Looking forward, this strategy offers promising potential for next-generation low-power, high-speed response, and multicolor for

dynamic devices. Future work will focus on optimizing material interfaces and ion transport pathways to further enhance switching uniformity and speed. However, achieving broader and more versatile color modulation remains challenging. Further studies on tailoring the color range of EC layers and coupling them with different underlying structural colors, or on introducing multiple EC modulation layers for multi-dimensional color modulation, could enable richer dynamic coloration; such integration currently poses considerable fabrication and compatibility difficulties. Nevertheless, this work establishes a viable platform for extending EC-structural color devices toward smart windows, adaptive optical systems, multifunctional photonic systems, etc.

4 Experimental

4.1 Structural color layers and electrochromic layers fabrication

The Ag/Al_2O_3/Ni/Al_2O_3 structural color multilayer was fabricated using e-beam evaporation, enabling precise control of film thickness and interface quality. Prior to deposition, glass substrates were ultrasonically cleaned and loaded into a high-vacuum chamber to suppress contamination. Ag reflective layer was first deposited as the optical backplane, followed by an Al_2O_3 dielectric layer. Subsequently, a thin Ni absorption layer and a final Al_2O_3 protective dielectric layer were deposited sequentially. The Al_2O_3 films were deposited at a vacuum of 1.5×10^{-2} Pa with an evaporation rate of 2.9 Å/s, while the Ni layer was deposited at 5.6×10^{-3} Pa with a rate of 2.9 Å/s. The thicknesses of all layers were precisely controlled to realize the designed FP resonance conditions.

For the EC stack, the ITO/WO_3/$LiTaO_3$/NiO/ITO layers were deposited under optimized conditions to ensure high optical transmittance, stable ion transport, and reliable electrochemical performance. The ITO layer was deposited at an evaporation rate of 6 Å/s, with a vacuum degree of 2.5×10^{-2} Pa, and an activated ion source (180 V, 3 A, Ar:O_2 = 5:15). The WO_3 layer was deposited at 5 Å/s (vacuum 2.5×10^{-2} Pa), the $LiTaO_3$ layer at 4 Å/s (vacuum 5×10^{-2} Pa), and the NiO layer at 4 Å/s (vacuum 5×10^{-2} Pa). Precise regulation of deposition rate, plasma conditions, and chamber stability throughout the entire process was essential for achieving uniform film quality and ensuring the stable, repeatable EC response of the device.

4.2 The logo of Northwestern Polytechnical University fabrication

The fabrication process was designed to construct a patterned device with a multi-layer functional structure, as illustrated in Fig. S11 in the ESM. First, an ITO transparent conductive film was uniformly deposited on the substrate, serving as the lower electrode. Then, spin coating of negative resist was applied to this ITO layer. A negative photolithography process was then used to selectively expose the lower electrode and the designated logo pattern area. Next, a layer of SiO_2 was deposited over the entire sample surface to provide ion isolation in the non-color-changing regions, assisting in optical modulation. The photoresist was subsequently removed via a stripping process, ensuring precise exposure of the logo pattern and lower electrode areas. In these regions, four functional layers—including the inorganic EC oxide layer (WO_3), all-solid-state electrolyte ($LiTaO_3$), ion storage layer (NiO), and counter electrode (ITO)—were sequentially deposited via e-beam evaporation. This process ensured precise control over the deposition and patterning of each layer, meeting the required optoelectronic performance and structural integrity of the final device.

Electronic Supplementary Material: Supplementary material (refractive indices of materials; optical simulation results under different structural parameters and incident angles; SEM and AFM characterizations of structural color and EC layers; cross-sectional SEM image of the entire device; visual comparison with simulated environmental backgrounds; schematic illustration of the logo-pattern fabrication process; comparison of EC devices' performance (Table S1); and supplementary videos) is available in the online version of this article at https://doi.org/10.26599/NR.2026.94908612.

Data availability

All data needed to support the conclusions in the paper are presented in the manuscript and the Electronic Supplementary Material. Additional data related to this paper may be requested from the corresponding author upon request.

Acknowledgements

This work was supported by the National Natural Science Foundation of China (Nos. 52475608, 52575659, and U23A20617), Natural Science Foundation of Ningbo Government (No. 2025J035, 2025QL057), Natural Science Foundation of Zhejiang Province (No. LQN25E050025), Ningbo Science & Technology Bureau Under Program Grant (No. 2025DJRC010008), Ningbo Youth Doctoral Innovation Project (No. 2023J396), and "3315 Program" Creative Teams of Ningbo (No. 2021A-041-C).

Declaration of competing interest

All the contributing authors report no conflict of interests in this work.

Author contribution statement

X. T. L.: Conceptualization, data curation, validation, experimental design, writing manuscript. J. C. Z.: Conceptualization, project administration, writing – review & editing. J. Y. Y.: Investigation, formal analysis. Y. H. G.: Investigation, validation. Y. H. H.: Experimental design, data curation. W. L. L.: Supervision, funding acquisition. Y. T. Y.: Project administration, funding acquisition, supervision, writing – review & editing. All the authors have approved the final manuscript.

Use of AI statement

None.

References

[1] Wang, Z.; Wang, X. Y.; Cong, S.; Geng, F. X.; Zhao, Z. G. Fusing electrochromic technology with other advanced technologies: A new roadmap for future development. *Mater. Sci. Eng.: R: Rep.* **2020**, *140*, 100524.

[2] Guo, J. K.; Jia, H. X.; Shao, Z. W.; Jin, P.; Cao, X. Fast-switching

WO_3-based electrochromic devices: Design, fabrication, and applications. *Acc. Mater. Res.* **2023**, *4*, 438–447.
[3] Kim, J.; Rémond, M.; Kim, D.; Jang, H.; Kim, E. Electrochromic conjugated polymers for multifunctional smart windows with integrative functionalities. *Adv. Mater. Technol.* **2020**, *5*, 1900890.
[4] Zhu, M. J.; Xu, B.; He, T. Z.; Elezzabi, A. Y.; Zhang, W.; Yu, W. W.; Chen, J. W. Smart electrochromic devices for wearables. *Adv. Mater. Technol.* **2025**, *10*, e01015.
[5] Gu, C.; Jia, A. B.; Zhang, Y. M.; Zhang, S. X. A. Emerging electrochromic materials and devices for future displays. *Chem. Rev.* **2022**, *122*, 14679–14721.
[6] Wu, W.; Wang, M.; Ma, J. M.; Cao, Y. L.; Deng, Y. H. Electrochromic metal oxides: Recent progress and prospect. *Adv. Electron. Mater.* **2018**, *4*, 1800185.
[7] Sun, X. H.; Wu, W.; Zhao, X. Y.; Qu, Z. Z.; Xu, K.; Zhang, X. Y.; Wang, B.; Rong, X. H.; Wang, X. W.; Wu, G. H. et al. Metal doping engineering of $W_{18}O_{49}$ for excellent dual-band electrochromic smart windows with integrated energy storage function. *Nano Res.* **2025**, *18*, 94907807.
[8] Li, X. T.; Zhao, J. C.; Yang, J. Y.; Huo, Y. H.; Yu, Y. T. Structural colors go active. *Adv. Sci.* **2025**, *12*, 2413027.
[9] Li, L.; Yu, Z. M.; Ye, C. Q.; Song, Y. L. Structural color boosted electrochromic devices: Strategies and applications. *Adv. Funct. Mater.* **2024**, *34*, 2311845.
[10] Wu, Y. K.; Chen, Y. M.; Song, Q. H.; Xiao, S. M. Dynamic structural colors based on all-dielectric Mie resonators. *Adv. Opt. Mater.* **2021**, *9*, 2002126.
[11] Wang, G. P.; Chen, X. C.; Liu, S.; Wong, C. P.; Chu, S. Mechanical chameleon through dynamic real-time plasmonic tuning. *ACS Nano* **2016**, *10*, 1788–1794.
[12] Eaves-Rathert, J.; Kovalik, E.; Ugwu, C. F.; Rogers, B. R.; Pint, C. L.; Valentine, J. G. Dynamic color tuning with electrochemically actuated TiO_2 metasurfaces. *Nano Lett.* **2022**, *22*, 1626–1632.
[13] Gugole, M.; Olsson, O.; Rossi, S.; Jonsson, M. P.; Dahlin, A. Electrochromic inorganic nanostructures with high chromaticity and superior brightness. *Nano Lett.* **2021**, *21*, 4343–4350.
[14] Tang, X. Q.; Hu, Z. S.; Wang, Z. Y.; Wu, X. Z.; Wang, Z.; Su, W. M.; Cong, S.; Geng, F. X.; Zhao, Z. G. Super-wide color tunability from a single electrochromic device through *in situ* reconstruction of optical cavity. *Adv. Mater.* **2025**, *37*, 2417511.
[15] Bian, C. C.; Wang, J. H.; Liu, H. H.; Yan, Y.; Zhang, P.; Yang, W. L.; Jia, S. S.; Guo, X. D.; Cai, G. F. Complementary multicolor electrochromic devices with excellent stability based on porous tin oxide nanosheet scaffold. *Nano Res.* **2024**, *17*, 3035–3042.
[16] Zhu, M. J.; Li, H. T.; Guo, Q. L.; Guo, J.; Wang, C. C. Electrically responsive photonic crystals with enhanced suspension stability and color saturation for electrophoretic displays and smart windows. *ACS Appl. Mater. Interfaces* **2024**, *16*, 32543–32553.
[17] Zou, C. J.; Komar, A.; Fasold, S.; Bohn, J.; Muravsky, A. A.; Murauski, A. A.; Pertsch, T.; Neshev, D. N.; Staude, I. Electrically tunable transparent displays for visible light based on dielectric metasurfaces. *ACS Photonics* **2019**, *6*, 1533–1540.
[18] Guo, J. K.; Jia, H. X.; Jin, P.; Huang, A. B.; Li, Z. S.; Shao, Z. W.; Ji, X. W.; Cao, C. C.; Gao, Q.; Cao, X. Transparent-to-reflective multicolor all-solid-state electrochromic devices for next-generation intelligent display windows. *Adv. Mater.* **2025**, *37*, e00350.
[19] Zhou, J. R.; Han, Y. G. Design of a widely adjustable electrochromic device based on the reversible metal electrodeposition of Ag nanocylinders. *Nano Res.* **2023**, *16*, 1421–1429.
[20] Wang, J. L.; Liu, J. W.; Sheng, S. Z.; He, Z.; Gao, J.; Yu, S. H. Manipulating nanowire assemblies toward multicolor transparent electrochromic device. *Nano Lett.* **2021**, *21*, 9203–9209.
[21] Zhang, X. C.; Sun, H. Z.; Li, Y.; Hao, J. H.; Liang, Q. H.; Zhang, Y. Y.; Wang, Y.; Li, X. W.; Zhang, X. P.; Ma, H. et al. Tunable structural colors based on grayscale lithography and conformal coating of VO_2. *Nanophotonics* **2025**, *14*, 1123–1133.
[22] Ke, Y. J.; Ruan, Q. F.; Li, Y. B.; Wang, H.; Wang, H. T.; Zhang, W.; Pan, C. F.; Nair, P. N. S.; Yin, J.; Yang, J. K. W. Engineering dynamic structural color pixels at microscales by inhomogeneous strain-induced localized topographic change. *Nano Lett.* **2023**, *23*, 5520–5527.
[23] Zhang, C.; Jing, J. X.; Wu, Y. K.; Fan, Y. B.; Yang, W. H.; Wang, S.; Song, Q. H.; Xiao, S. M. Stretchable all-dielectric metasurfaces with polarization-insensitive and full-spectrum response. *ACS Nano* **2020**, *14*, 1418–1426.
[24] Dai, C. J.; Wang, Z. J.; Shi, Y. Y.; Li, Z.; Li, Z. Y. Scalable hydrogel-based nanocavities for switchable meta-holography with dynamic color printing. *Nano Lett.* **2022**, *22*, 9990–9996.
[25] Dong, D. M.; Wang, W. W.; Rougier, A.; Dong, G. B.; Da Rocha, M.; Presmanes, L.; Zrikem, K.; Song, G.; Diao, X. G.; Barnabé, A. Life-cycling and uncovering cation-trapping evidence of a monolithic inorganic electrochromic device: Glass/ITO/WO_3/$LiTaO_3$/NiO/ITO. *Nanoscale* **2018**, *10*, 16521–16530.
[26] Li, W. J.; Zhang, X.; Chen, X.; Zhao, Y. M.; Wang, L. B.; Chen, M. J.; Li, Z. T.; Zhao, J. P.; Li, Y. Lithiation of WO_3 films by evaporation method for all-solid-state electrochromic devices. *Electrochim. Acta* **2020**, *355*, 136817.
[27] Xiao, Y. J.; Zhang, X.; Yan, D. K.; Deng, J. B.; Chen, M. J.; Zhang, H. L.; Sun, W. H.; Zhao, J. P.; Li, Y. Defect engineering of W^{6+}-doped NiO for high-performance black smart windows. *Nano Res.* **2024**, *17*, 3043–3052.
[28] Jiang, C. Y.; Ge, R.; Bian, C. C.; Chen, L. R.; Wang, X. R.; Zheng, Y.; Xu, G.; Cai, G. F.; Xiao, X. D. Multicolored inorganic electrochromic materials: Status, challenge, and prospects. *Nanoscale* **2023**, *15*, 15450–15471.
[29] Liu, Q. R.; Chen, Q. Q.; Zhang, Q. Q.; Dong, G. B.; Zhong, X. L.; Xiao, Y.; Delplancke-Ogletree, M. P.; Reniers, F.; Diao, X. G. Dynamic behaviors of inorganic all-solid-state electrochromic device: Role of potential. *Electrochim. Acta* **2018**, *269*, 617–623.
[30] Zhang, Y. Q.; Ding, Y. L.; Lan, F.; Zhang, W. J.; Li, J. F.; Zhang, R. F. Recent advances in tungsten oxide-based chromogenic materials: Photochromism, electrochromism, and gasochromism. *Nanoscale* **2024**, *16*, 21279–21293.
[31] Zhai, Y. L.; Li, J. H.; Shen, S.; Zhu, Z. J.; Mao, S.; Xiao, X.; Zhu, C. Z.; Tang, J. G.; Lu, X. Q.; Chen, J. Recent advances on dual-band electrochromic materials and devices. *Adv. Funct. Mater.* **2022**, *32*, 2109848.
[32] Zhang, Y. Q.; Ding, Y. L.; Lan, F.; Zhang, W. J.; Zhao, S. M.; Huang, Y.; Li, R.; Li, J. F.; Zhang, R. F. A photo- and electrochromic dual-responsive smart window for full-day photothermal management. *Small* **2025**, *21*, 2501977.
[33] Zhu, T. X.; Xiong, J. Q.; Chen, J. W.; Zhou, X. R.; Cai, G. F.; Lai, Y. K.; Lee, L. S. Flexible electrochromic fiber with rapid color switching and high optical modulation. *Nano Res.* **2023**, *16*, 5473–5479.
[34] Liu, L.; Du, K.; He, Z. B.; Wang, T.; Zhong, X. L.; Ma, T.; Yang, J. M.; He, Y. C.; Dong, G. B.; Wang, S. H. et al. High-temperature adaptive and robust ultra-thin inorganic all-solid-state smart electrochromic energy storage devices. *Nano Energy* **2019**, *62*, 46–54.
[35] Chen, M. J.; Deng, J. B.; Zhang, H. L.; Zhang, X.; Yan, D. K.; Yao, G. X.; Hu, L. P.; Sun, S. K.; Zhao, J. P.; Li, Y. Advanced dual-band smart windows: Inorganic all-solid-state electrochromic devices for selective visible and near-infrared modulation. *Adv. Funct. Mater.* **2025**, *35*, 2413659.
[36] Chen, M. J.; Zhang, X.; Sun, W. H.; Xiao, Y. J.; Zhang, H. L.; Deng, J. B.; Li, Z. T.; Yan, D. K.; Zhao, J. P.; Li, Y. A dual-responsive smart window based on inorganic all-solid-state electro- and photochromic device. *Nano Energy* **2024**, *123*, 109352.
[37] Zhang, T. Y.; Mu, X. Y.; Li, Y. W.; Cong, S.; Zheng, S. N.; Huang, R.; Geng, F. X.; Zhao, Z. G. Optical-cavity-incorporated colorful all-solid-state electrochromic devices for dual anti-counterfeiting. *Adv. Mater.* **2024**, *36*, 2402670.
[38] Sun, W. H.; Zhang, X.; Zhang, H. L.; Ren, Z. C.; Chen, M. J.; Xiao, Y. J.; Li, Z. T.; Deng, J. B.; Yan, D. K.; Zhang, L. P. et al. Statically

multiple colors and dynamically infrared emissivity modulation compatible electrochromic devices via simple fabry-perot photonic structures. *Laser Photonics Rev.* **2023**, *17*, 2300476.

[39] Chen, J.; Wang, Z.; Chen, Z. G.; Cong, S.; Zhao, Z. G. Fabry-perot cavity-type electrochromic supercapacitors with exceptionally versatile color tunability. *Nano Lett.* **2020**, *20*, 1915–1922.

[40] Wu, Q.; Wang, X. Y.; Sun, P. Y.; Wang, Z.; Chen, J.; Chen, Z. G.; Song, G.; Liu, C. L.; Mu, X. Y.; Cong, S. et al. Electrochromic metamaterials of metal-dielectric stacks for multicolor displays with high color purity. *Nano Lett.* **2021**, *21*, 6891–6897.

[41] Wang, Z.; Wang, X. Y.; Cong, S.; Chen, J.; Sun, H. Z.; Chen, Z. G.; Song, G.; Geng, F. X.; Chen, Q.; Zhao, Z. G. Towards full-colour tunability of inorganic electrochromic devices using ultracompact fabry-perot nanocavities. *Nat. Commun.* **2020**, *11*, 302.

[42] Lee, Y.; Herbig, J.; Arslan, S.; Ludescher, D.; Ubl, M.; Georg, A.; Hentschel, M.; Giessen, H. Inorganic electrochromic metasurface in the visible. *Nano Lett.* **2025**, *25*, 7553–7559.

[43] Hail, C. U.; Schnoering, G.; Damak, M.; Poulikakos, D.; Eghlidi, H. A plasmonic painter's method of color mixing for a continuous red-green-blue palette. *ACS Nano* **2020**, *14*, 1783–1791.

[44] Qiu, J. J.; Gao, F.; Jiang, X. Y.; An, T.; Shi, N.; Fan, T. X.; Zhao, Q. B. Structural color palettes from colloidal color mixing. *J. Mater. Sci.* **2025**, *60*, 5914–5924.

[45] Simonot, L.; Hébert, M. Between additive and subtractive color mixings: Intermediate mixing models. *J. Opt. Soc. Am. A* **2014**, *31*, 58–66.

[46] Kats, M. A.; Blanchard, R.; Genevet, P.; Capasso, F. Nanometre optical coatings based on strong interference effects in highly absorbing media. *Nat. Mater.* **2013**, *12*, 20–24.

[47] Park, C. S.; Shrestha, V. R.; Lee, S. S.; Kim, E. S.; Choi, D. Y. Omnidirectional color filters capitalizing on a nano-resonator of Ag-TiO_2-Ag integrated with a phase compensating dielectric overlay. *Sci. Rep.* **2015**, *5*, 8467.

[48] Wen, R. T.; Granqvist, C. G.; Niklasson, G. A. Eliminating degradation and uncovering ion-trapping dynamics in electrochromic WO_3 thin films. *Nat. Mater.* **2015**, *14*, 996–1001.

[49] Santosa, A. S. S.; Chang, Y. W.; Dahlin, A. B.; Österlund, L.; Volpe, G.; Xiong, K. L. Video-rate tunable colour electronic paper with human resolution. *Nature* **2025**, *646*, 1089–1095.

[50] Buch, V. R.; Chawla, A. K.; Rawal, S. K. Review on electrochromic property for WO_3 thin films using different deposition techniques. *Mater. Today: Proc.* **2016**, *3*, 1429–1437.